Ionics (2019) 25:1793–1803
https://doi.org/10.1007/s11581-018-2625-0

ORIGINAL PAPER

Effect of synthesis parameters on tuning of phase and shape of hierarchical iron oxides and selective application as supercapacitor

Rasmita Barik[1] · Nafiseh Moghimi[2] · Kam Tong Leung[2] · Mamata Mohapatra[1]

Received: 26 March 2018 / Revised: 17 May 2018 / Accepted: 4 June 2018 / Published online: 5 July 2018

Abstract

The synthetic strategy for iron oxides with diverse superstructures has become one of the most promising researches due to their advance and synergistic application in energy and environment field. Self-assembling of nanostructure to structural hierarchy in general enhances mass transportation, reducing resistance to diffusion, and high surface areas for adsorption and electrochemical reaction, and thus much effort has been devoted to the exploration of various novel synthesis schemes for high-throughput synthesis processes with a choice of starting materials. In this strategy, we utilize metal-organic solvent solutions as the starting material for synthesizing functional hierarchical iron oxide materials without further addition of base for hydrolysis reactions. The process is templates/surfactant less which makes the process simple without intact of other impurities in desired structure. The agglomerations of the particles are also controlled due to acidic pH condition adopted during synthesis. All the experiments were done at a moderate temperature (~< 100 °C) with a variation of time and concentration. The reaction parameters are optimized to get uniform and highly dispersed flower or spindle-shaped 3D hierarchical goethite phase and thereof we evaluate the electrochemical capacitance using cyclic voltammetry technique. One of the pure iron oxide samples shows specific capacitance value of 243.2 Fg^{-1} and exhibited 26 Wh Kg^{-1} energy density at 0.5 Ag^{-1} current density.

Keywords Hierarchical · Self-assembling · Flowery structured · Specific capacitance

Introduction

Hierarchical, self-assembly of nanocrystals having high surface area and narrow particle size distribution has high impact in scientific field for advance applications due to active domain on their surfaces. Tailoring and shaping up nanostructures by various synthetic approaches create new province of applications. For anticipated advance applications, the materials with better performances/safety/costs are needed [19, 21]. The development or the discovery of new electrode materials to ensure a hike in performance is required. Electrochemical reactions, adsorptions, and heterogeneous catalytic reactions are shape and surface dependent which is mainly responsible to enhanced microscopic/electroactive surface area [18, 45]. Therefore, the manipulation of synthetic approach through controlled chemical reactions for the fabrication of high surface area and surface-modified well-defined nanostructured metal oxides were very often explored [12, 25, 43]. Particularly, nanosized iron oxide materials with diverse morphologies and dimensions have been synthesized through various modified synthetic routes to control both phase, shape, size, and surface area and investigated them in myriad of applications including supercapacitors [3, 36], lithium ion battery [6, 42], catalysis/adsorptions [4, 34, 37], and electrochemical sensors [28, 35]. Recently, the research is projected to get iron oxide with delicate morphologies by low-dimensional assembling of nano-scaled material into unique three-dimensional (3D) hierarchical superstructures for tuning many morphology-dependent advance applications [20]. For example, [47] reported development of 3D urchin-like superstructures of α-Fe_2O_3 nanorods by template free and facile

Electronic supplementary material The online version of this article (https://doi.org/10.1007/s11581-018-2625-0) contains supplementary material, which is available to authorized users.

✉ Mamata Mohapatra
mamatamohapatra76@gmail.com

Rasmita Barik
rasmitabarikimmt@gmail.com

[1] Hydro and Electrometallurgy Department, CSIR-Institute of Minerals and Materials Technology, Bhubaneswar 751013, India

[2] WATLab, Department of Chemistry, University of Waterloo, Waterloo, ON N2L 3G1, Canada

precipitation method which showed improved sensing performances towards ethanol. [46] followed the ethylene glycol-mediated process to synthesize uniform and self-assembled 3D flower-like iron oxide from ferric chloride for removing toxic heavy metals. Similarly, flower-like α-Fe_2O_3 was developed using [1] ferric chloride and sodium sulfate under hydrothermal condition nanostructures for hydrogen gas sensors at room temperature. Hierarchical α-FeOOH porous nanoparticles were organized and prepared via a facile polystyrene (PS) microsphere template method [9] for adsorption and photo degradation of Rhodamine B under UV light at room temperature. However, involvement of high temperature process, surfactant/organic, causes release of potential process-related risk to the medium and also lowers the yield of the product. Due to the polycationic species available at the molecular level, the iron oxides perform fast hydrolysis and condensation to form highly reactive ferric complexes [39]. Thus, the synthesis of mesostructure renders a substantial challenge for economical and an environmentally friendly method with controlled surface morphology. The designing of 2D and 3D architectures by control over the metal ligand coordination sphere and ligand through self-assembly process was possible. The synthesis of inorganic hierarchical/complex structures with ideal crystal growth behaviors and controlled fabrication of inorganic hierarchical/complex structures with uniform morphology and size was one of the major or key factors. Kinetic of hydrolysis of coordinated metal cation with strong complexing polydentate ligands by more than one bond could be slowed down. For example, coordinating groups such as polycarboxylate or amino ligands [16, 24, 39] were reported to control the iron hydrolysis to some extent.

The diminution of natural fossil fuels and escalation in global warming creates the space for green clean renewable energy sources which can supplement and replace the conventional energy sources. Different metal oxides were tested for alternative energy sources like supercapacitors or batteries. The clean energy technologies are useful for next-generation energy devices, hybrid electric vehicles, and biomedical applications [44]. Recently, different iron oxides and hydroxides (Fe_2O_3, Fe_3O_4, FeOOH) have drawn attention as alternative energy source due to their high theoretical capacitance, wide operating potential window, low cost, and natural abundance. [3, 5, 7, 30, 40]. Asymmetric and hybrid supercapacitors (HSCs) were extensively studied for energy storage with high energy density. As the asymmetric capacitors have both faradaic double and capacitive electrodes which results in high energy density of the metal oxides. There are two types of supercapacitors, i.e., electric double layer and pseudo-capacitors. Electric double layers are having high surface area and high conductivity value whereas pseudo-capacitors give more capacitance due to the redox reactions at the surface of the electrodes. But still, it is a challenge to develop nanomaterials with high capacitance, good rate capability, and excellent cycling stability.

Herein, coordination-mediated complex hydrolysis of iron oxide was achieved by the controlled hydrolysis and assembly of molecular precursors in the solution–complex interface without structure-directing surfactants into the 3D frameworks with hierarchical structure. Here, the solvent 2-methoxy ethanol serves as ligand and hydrolyzing reagent at low temperature. The present study deals with methodical investigation of the effect of experimental conditions on the selective phase formation and morphology of the α-FeOOH precursors and the formation reaction mechanism. Furthermore, for the nano-flower iron-oxide composites with nafion on glassy carbon electrode was investigated to evaluate electrochemical capacitance. The capacitance of this nano-flower iron oxide electrode was quite comparable with other reported electrodes. The present work will be helpful for the easy and effective development of iron oxide nanostructures and enhance the prospects for the iron oxide synthesis and electrochemical applications.

Experimental section

Chemicals and synthesis

$Fe(NO_3)_3{\cdot}9H_2O$ (E-Merck, India), and ethylene glycol mono methyl ether ($CH_3O{\cdot}CH_2{\cdot}CH_2{\cdot}OH$) (EGME) (E-Merck, India) were used for iron oxide synthesis. The iron oxides were synthesized by adopting our reported synthesis method [3]. Standard solutions of metal salts in deionized water were prepared, and these solutions were used in different stoichiometric amounts for precipitation work. Hierarchical α-FeOOH precursors were developed by a solution-based sol-gel method. The required amount of different solution was taken in three naked flask equipped with condenser. The solution was stirred for 15 min and pH was monitored. Then, the required amount of EGME solution was added and stirred at speed of 400 rpm by maintaining required temperature. The ratio of the salt solution to solvent was varied with four different ratios of 1.5:1, 1:1, 1:2, 1:4, and 1:6. The pH was also monitored after the precipitation was completed. The precipitation kinetics was monitored by carrying out the precipitation at various times under affixed ratio of solvent to salt solution. After cooling, the slurry was centrifuged and washed several times with distilled water and absolute alcohol. Then, the powders were dried at room temperature.

Characterization

Different phases and crystal structures are determined by X-ray diffraction in PAnalytical model X'Pert PRO PW-3040/60 with Mo-Kα radiation (λ = 0.709) at a scan speed of

1.2° min^{-1} over a range of 5 to 40°. Raman spectra were obtained by Renishaw (Renishaw plc, Gloucesteshire, UK) via Micro Raman spectrophotometer. The instrument was equipped with 514 nm green laser having 1 cm^{-1} spectra resolution of Raman shift, X-Y step resolution of 0.1 μm, and confocal resolution of 2.5 μm. The nano-architectures were obtained through an electron microscope (FEI, TECNAI G^2 20, TWIN) and transmission electron microscopy (TEM). Selected area electron diffraction (SAED) patterns and EDAX were also evaluated. The surface area of the nanomaterials was analyzed with Quantachrome 1750 with ASiQ-WiN and Autosorb-iQ device surface area analyzer by nitrogen absorption–desorption method. Chemical state of iron oxide material was analyzed by X-ray photoelectron spectroscopy (XPS) in a Thermo-VG Scientific ESCALab 250 Microprobe, equipped with a monochromatic Al Kα X-ray source (1486.6 eV).

Electrochemical measurement

All the electrochemical tests were performed by three-electrode cell using a Biologic SP-300 electrochemical analyzer. Cyclic voltammetry studies were obtained by using three-electrode system as iron oxide on glassy carbon as working electrode, a platinum electrode, and Ag/AgCl as the reference electrode in the potential range of 0 V to 0.85 V at a sweep rate of 5–100 mVs^{-1}. All the electrochemical tests were carried out by 1 M KOH. The synthesized materials were dispersed over a glassy carbon electrode with carbon black, 2% Nafion, and dried prior to the electrochemical experiments. The working electrode was prepared by the ratio of 90:8:2 ratio of active material/carbon black/nafion. Charge–discharge tests were performed using chrono-potentiometric method. EIS (electrochemical impedance spectroscopy) was studied though an open circuit at ac voltage of 5 mV in 1 M KOH electrolyte and the Nyquist plots were obtained in the frequency range of 10 mHz to 100 Hz.

Results and discussion

Effect of solvent on phase formation using different ratio of salt solution: solvent

Since there was no surfactant or capping agent in the present synthesis, the solvent employed in the system is playing an important part for the formation of the precursors. Precipitation of iron oxide by varying temperatures at 80 and 100 °C using different ratio of salt solution/solvent. Precipitation was completed within 5 h of reaction time. However, there was large difference in the percentage of iron (iron is only present as Fe^{3+}) in the prepared solid samples. It was observed that initially, at 5 h of reaction time, only 17% of ferrous ion was present in the solution which was almost absent during further aging of the solution. However, in the present report, we detect Fe^{2+} in the solution during an initial period of reaction. Therefore, EGME will act as a mild reducing reagent before complexing with iron solution. The percentage of iron (iron is only present as Fe^{3+}) in the precipitated products varied from 55 to 62%. Such variation may be due to the presence of different phases or due to adsorbed/intercalated water molecule. The crystal structure of the precipitates was studied by XRD analysis. The XRD patterns of the product prepared at 80 and 100 °C at different time intervals are shown in Fig. 1. To understand the effect of EGME on phase formation, a series of other investigations were carried out up to 5 h by varying the ratio of Fe/EGME solution both at 80 and 100 °C. As shown in Fig. 1, the patterns obtained at 80 and 100 °C for the sample prepared at 1.5:1 ratio showed crystalline goethite phase with increase in concentration of iron and synthesis temperature. The result revealed higher reaction activity at higher temperature. The diffraction peaks of the samples could be indexed to orthorhombic α-FeOOH (goethite, G) and Fe_5O_7 ($OH{\cdot}4H_2O$ (ferrihydrite, F) (ICSDS reference code 00-002-0272 and 00-029-0712, respectively). Finally, at 100 °C, almost all the peaks were indexed to an orthorhombic phase of goethite (space group Pb nm, no. 62). However, increasing temperature to 100 °C for 5 h of reaction time, the XRD pattern matched to complete goethite phase.

Significant broadening of the diffraction peaks indicated that the goethite is of nanosize. As mentioned earlier, EGME

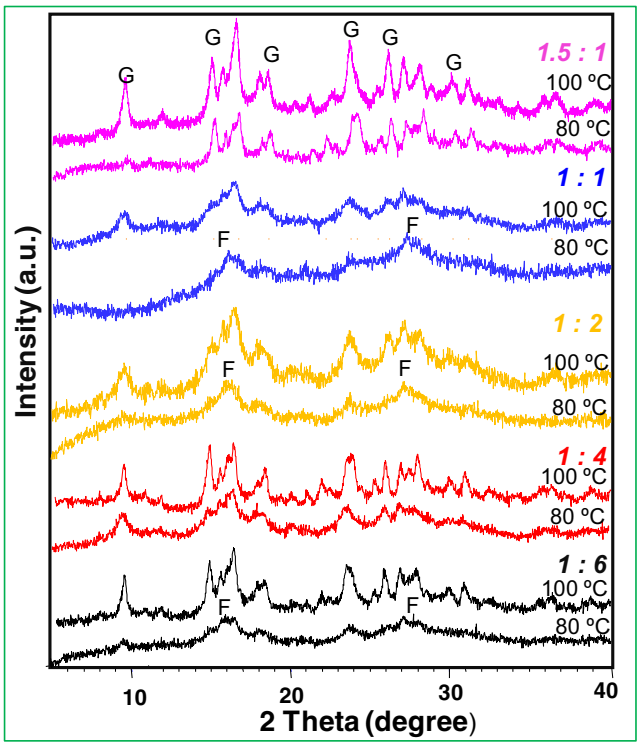

Fig. 1 XRD patterns of different synthesized samples

also acted as reducing ligand which exhibited associative interactions with interfacial iron sites of ferrihydrite. It appears that solvent made these sites to more labile sites thus facilitating the transformation to goethite, possibly in conjunction with enhanced dissolution of ferrihydrite. During the reaction, pH of the solution varied only within 0.5 units as compared to initial solution pH. Thus, temperature had significant role in the transformation of metalo-organic polymeric complex to pure goethite phase and also in controlling the redox reaction during hydrolysis of metal complex solution. According to partial-charge model [31], hydrolysis of iron occurred through the formation of aqua or aqua-hydroxo complexes when pH of the solution is less than 7. The aqua complex also transformed to hydroxo complex after protonation. However, in the presence of solvent, iron gets solvated and could be complexed with the anion present in the solution. Their reactivity depends on the dielectric and structural properties of the solvent, association equilibrium for chelate formation, and the relative rates of solvent loss from the solvent cation []. Here, the complexes formed between Fe(III) ions and EGME molecule may favor the formation of the planar tetramer $[Fe_4(OH)_{12}(OH_{24})]$. Then, embryos of double chains of octahedra, characteristic of the structure of goethite, might be formed due to condensation through olation process. Thus, the formation of goethite was facilitated through this solvent. Therefore, the process is faster than the usual method.

However, by increasing Fe/EGME ratio to 1:1, the two-line ferrihydrite was obtained both at 80 and 100 °C reported in our previous work. Likewise, the solvent to precursor ratio was varied again 1:2 and 1:4 but increase in solvent ratio, the crystallinity of the sample was increased slowly, and at 1:6 ratio, formation of goethite occurred at 100 °C [3]. The intensity of peaks of different planes and their corresponding ratios were different for different samples. This might be due to the particle orientation in different planes because of the complex nature of the solution and of changing the nucleation and growth mechanism.

Therefore, increase of solvent concentration during synthesis has significant effect on the phase formation. It was also observed that the difference in pH of the precursor and final solution was increased gradually as the solvent concentration changed. Decrease in pH encouraged the conversion of two-line ferrihydrite to goethite by enhancing the solubility and dissolution of ferrihydrite. It is assumed that when the ferric ion concentration is more, the complex formed between EGME and Fe(III) might be encapsulated on the $Fe(OH)_3$, and the possibility of the particle transformation from complex into a specific oxy-hydroxide phase was more than the phase transformation of the $Fe(OH)_3$ particles as reaction proceeds. The phases of iron oxide/hydroxide crystals grown in this way would depend on the surface energy of the crystal particle, which changed as the particles grow [15, 33]. Hence, the resulting phase was particularly sensitive to the ionic strength of the solution. In that composition, the starting $Fe(NO_3)_3$ solution would increase both the ionic strength and the ferric ion concentration, and together, these two factors would determine the ferric ion solvation (or hydration) stabilities. While increasing further the concentration of solvent, the other properties such as viscosity, conductivity, and hydrogen bonding capacity of the solvent play a major role to determine the fate of nucleation path. Hence, selectively goethite was formed at higher temperature. With the increase of solvent, the mechanism may differ and slow down due to the ligand behavior of the solvent. Further increasing the concentration of solvent, the viscosity, conductivity, and hydrogen bonding capacity of the solvent would play a major role for the determination of the fate of nucleation path. This type of observation had already been reported during the incorporation of foreign ion in octahedral matrix of goethite [14].

From the XRD patterns, we had observed that the peak intensities of goethite phases and ferrihydrite were different for different precursor which might have some effects on the particle orientation and their microstructures. The proposed particle growth mechanism could also explain the different crystal orientation and assemblies observed in the following sections. Raman spectra support the phase formation of nano-iron oxides as given in supporting data S1.

The morphological and structural features of the synthesized samples were examined by TEM (Fig. 2) and FESEM (Fig. S2). Figure 2 shows typical TEM along with graphical patterns obtained from different precursors at 80 and 100 °C, respectively. From the TEM images of the sample obtained with salt/solvent concentration ratio of 1.5:1 at 80 °C, both nanospherical particle and rod-shaped particles were being observed, whereas mostly nanorod along with very few nanospherical particles were observed for the sample obtained with similar precursor at 100 °C. At low temperature, the ferrihydrite particles dominated while the same at higher temperature showed clearly a rod shape of 50–150 nm length goethite particle surrounded by very small amount of aggregated 1–5 nm tiny particles. The microstructure at salt/solvent ratio 1:1 under similar condition showed porous spindle-like structure resembling thin sheets due to aggregation of very tiny spherical nanoparticles. On further increasing, the temperature thin sheets assembled to form irregular flower shape.

TEM pictures obtained at salt/solvent ratio 1:2 and 1:4 at 80 °C showed completely different morphology and two different particles. One was nanorod and the other was nano-hierarchical morphology that was separately growing, which indicated the hierarchical has been started and the growth and conversion of one phase to the other phase also started. The sample was more or less assembled in the shape of mushrooms, and in the following secondary growth stage, the primary particles aggregated into spindle-shaped particles which became the core of the flower-like structure. They continued to grow by combining with the remaining primary particles

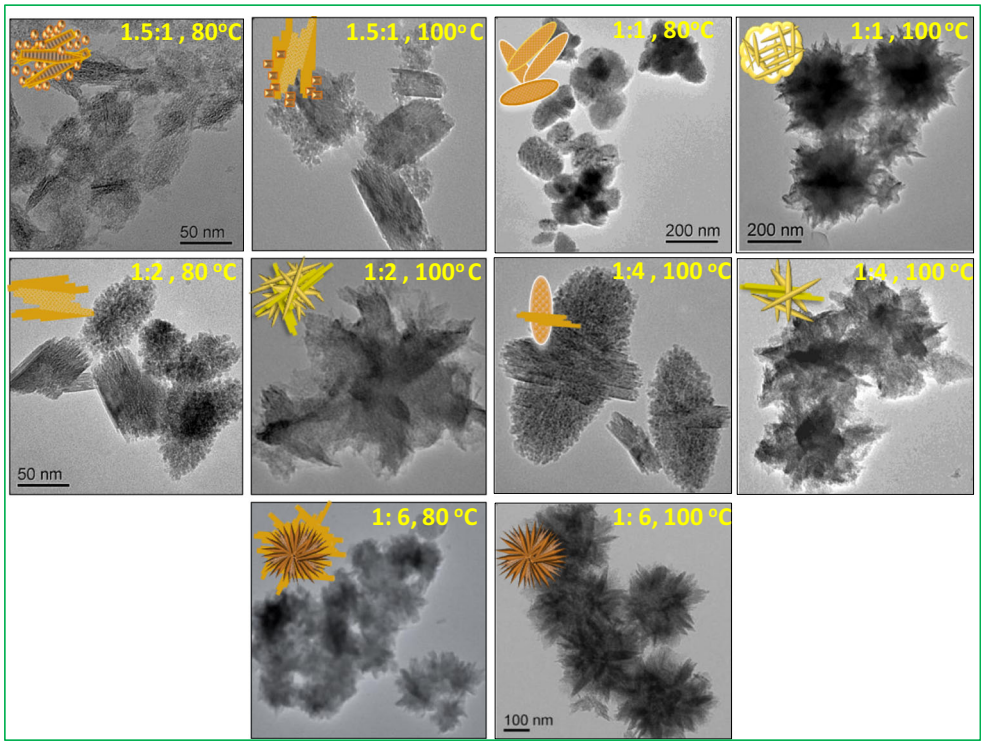

Fig. 2 TEM micrographs of as-prepared iron oxide samples at different salt/solvent concentration all after 5 h reaction time. 1:1, 100 °C and 1:6, 100 °C. The TEM images are reported in [3]

and forming the intermediate phase of flower-like precursors. The complete urchin-like morphologies could be observed clearly at higher temperature under similar condition.

The surface of the nanosheets in the flower-like structure was very smooth, probably due to Ostwald ripening. The urchin shape was quite definite and sharp on further increasing of solute/solvent ratio to 1:6; hierarchical morphology of the nanoparticles was observed. From the TEM picture, the presences of pores were also felt. This phenomenon could help in understanding the tiny misalignments in the flower crystalline structure. The role of the solvents in the formation of the complex flower-shaped structure seems decisive. The TEM pictures obtained for the sample at 1:6 ratio at 100 °C showed complete flower-like morphologies. The 1:1 and 1:6 sample was already reported in our previous publication [3]. Most of the flowers showed an inner contrast variation, suggesting the existence of a core/shell structure, consistent with one form of iron oxide in core coated with another form of iron oxide. Figure 3a represents the schematic presentation of all the materials corresponded to TEM analysis.

During the precipitation reaction, the surface or sub-surface Fe ions of low coordination were frequently missing due to chelation or surface complexation []. Thus, the surface was well hydroxylated in aqueous medium and may develop a well-ordered layer of water molecules []. All these factors may affect the surface energies and morphologies. Therefore, the shape anisotropy developed by side-by-side rod aggregation, presumably driven by minimizing the total energy of the nano-system, and thus develop a planar stacking along specific crystal planes through inherent van der Waals attraction observed on α-FeOOH single crystals [29, 41], facilitated by a high degree of freedom for rotation and translation movement (i.e., Brownian motion) in aqueous solutions. Schematic mechanism of ligation and hydrolysis of Fe(III) solution in presence of EGME was shown in Fig. 3b. The truncated pseudo prismatic shape as shown in TEM images was grown when the particle surface was enclosed by (100) and (011) surfaces, and their stability enhanced when the (100) surface was cleaved along the hydroxylated plane []. The aspect ratio of OH-terminated truncated bipyramids again was lower. Figure 3c summarizes the possible evolution from truncated bipyramid seeds to flowery shape under a kinetically controlled synthesis. Under suitable conditions, spindle-like particle with the (111) oriented trunk and branches could be formed and then truncated pseudo prismatic-shaped particle, with each arm extending along the (110) direction, might be formed. This may further evolve into threefold symmetric branches. Finally, from polycrystalline or multiple twined particles with surface asperities, flowers were formed.

The nitrogen adsorption–desorption isotherm was performed within the region of 0 to 1 relative pressure (P/P_0). For the 1.5:1, 80 °C material, the adsorption–desorption isotherm curve and pore size distribution curves are given in Fig. 4. The isotherm exposes the type IV nature, of material with mesoporosity. The BET surface area was calculated as 54.04 $m^2\ g^{-1}$. The Barrett–Joyner–Halenda (BJH) method was obtained to calculate pore size distribution. The calculated pore diameter and pore volume from the pore size distribution

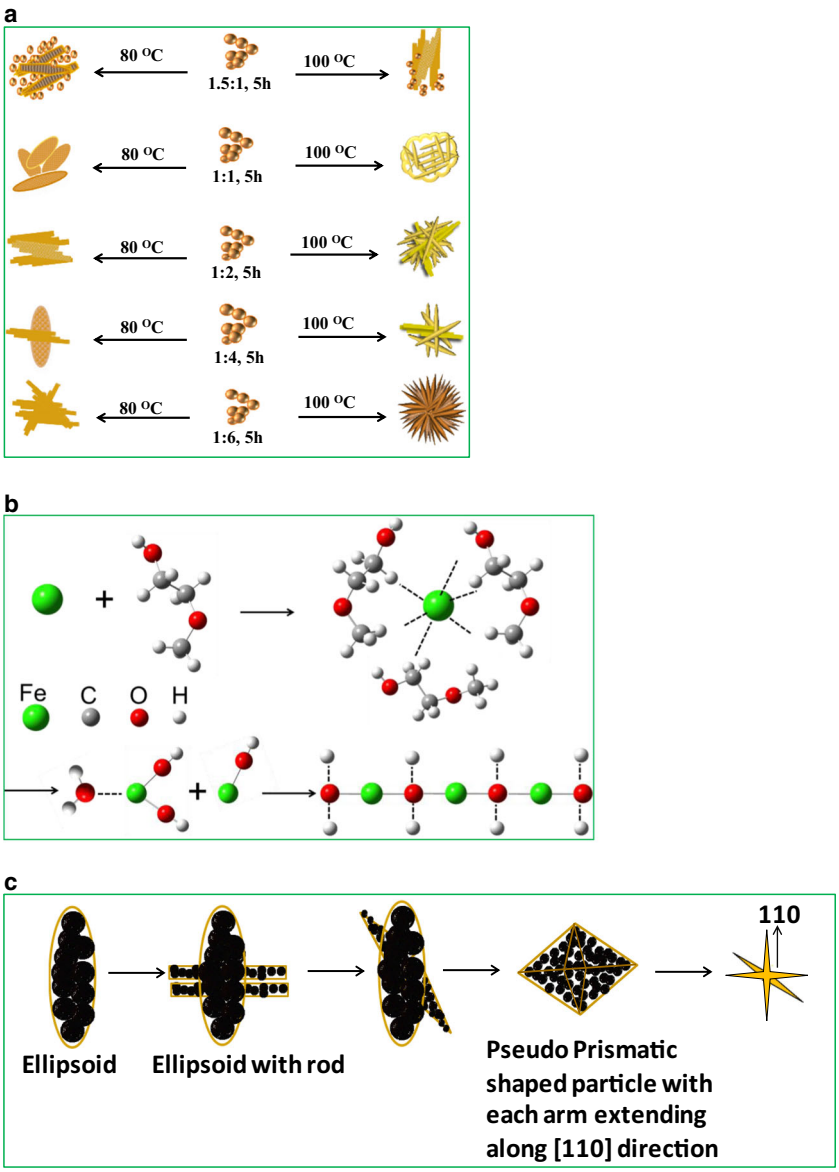

Fig. 3 **a** Schematic diagram for nucleation and growth evolution of nano iron oxide samples at different salt:solvent concentration. **b** Schematic mechanism of ligation and hydrolysis of Fe(III) solution in presence of EGME. **c** Schematic presentation of growth of 3D iron nanostructure from ellipsoid shape to nano-flowers

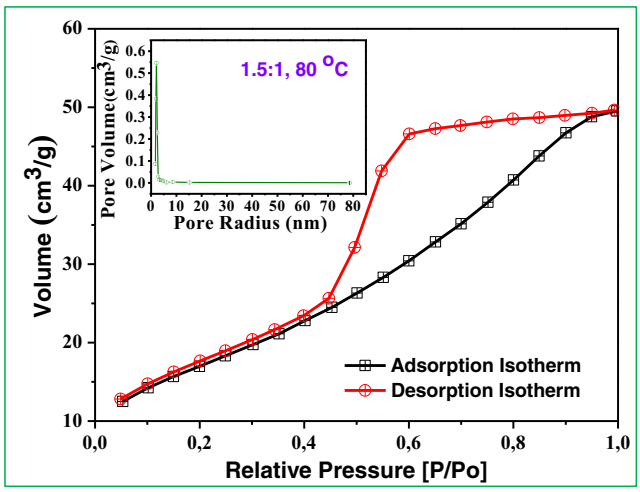

Fig. 4 Surface area and pore size distribution graphs (inset) for 1.5:1, 80 °C sample

curve (S_2 inset) are 8.76 nm and 0.99768 $cm^3\ g^{-1}$, respectively. The observed hysteresis loop shifted to a higher relative pressure on approaching P/P0 = 1, suggesting the presence of mesoporous a low degree of aggregation, which is confirmed by TEM images.

The chemical state and the electronic structures of 1.5:1, 80 °C material with goethite phase was analyzed by X-ray photoemission spectroscopy (XPS). The main composition of the iron oxide material Fe, O, and C peaks were found in survey of the XPS spectrum as shown in Fig. 5a. The different electronic states of Fe 2p with high-resolution curve-fitted XPS spectrum was given in Fig. 5b. The characteristic peaks of Fe $2p_{1/2}$ at 711.4 eV and Fe $2p_{3/2}$ at 725.2 eV were observed, with a prominent satellite peak at 719.1 eV. These broad peaks were obtained due to the electrostatic interactions between the Fe2p and unpaired Fe3d electrons, resulting in

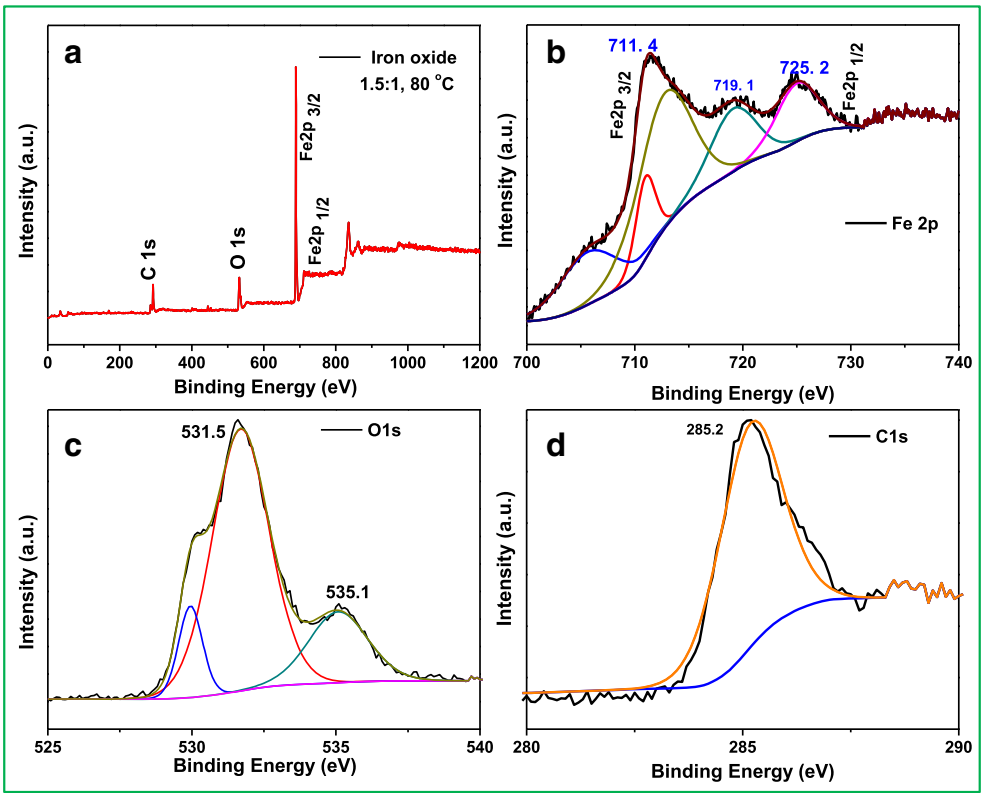

Fig. 5 Chemical state analysis. **a** Survey spectra of as-prepared iron oxide with ratio 1.5:1 at 80 °C. **b** Fe2p. **c** O1s. **d** C1s

spin–orbit coupling and crystal field interactions [2, 3]. There were two binding energy peaks observed at 531.5 and 535.1 eV in the O1s region respectively, which can be assigned to oxygen atoms in the iron oxide lattice, and O1s (Fe–O) is shown in Fig. 5c. Peak (531.5 eV) was assigned to lattice hydroxyl group of O1s (Fe–OH lattice), which signifies the formation of Fe–O–Fe bond, Fe–O–H bond, and H–O–H bond. The C1s spectrum is observed at 285.2 eV corresponding to sp^2 carbon as shown in Fig. 5d. From the above study, it was suggested that the FeOOH formed by the adsorption of Fe–OH on the surface after oxidation [17, 27].

Electrochemical properties Cyclic voltammetry measurements were conducted to test the supercapacitor performance of various phases of as-synthesized iron oxide nanostructured materials (obtained at different ratio of Fe/EGME at 80 and 100 °C and 5 h). Figure 6a represents the CV curves of the electrodes at a scan rate of 5 mVs^{-1} in a three-electrode cell at potential window of 0.0 to 0.85 V in 1 MKOH electrolyte. Most of the samples show an obvious redox peak (0.2–0.4 V), which was observed in the redox process. It can be attributed to the reduction of Fe^{3+} to Fe° and reversible reaction with the electrolyte. Meanwhile, no peak is recorded for the sample obtained at Fe/EGME = 1.5:1 at 100 °C, which showed the highest current density indicating the double-layer capacitance behavior. But according to the current density, the 1.5:1 at 80 °C material showed the highest value. This may be due to the morphological predominance of spherical particle. It has been already reported that the specific capacitance values of spherical particles is more than that of the rod-shaped particles [8, 38]. Therefore, the 1.5:1 at 80 °C material was used for further detailed electrochemical study. The presence of more no. of Fe^{+3} ions participate in faradic reactions and showed pseudo-capacitive behavior. This could probably be due to very fast faradaic process at the electrode indicating the dominance of pseudo-capacitance over double-layer capacitance process [22]. By comparing both the CV curves at fixed scan rate, it was observed that the current is highly larger with much larger integrated area in case of the sample obtained at lower temperature revealing higher capacity and faster kinetics for transformation in the electrode. This may be due to difference in adsorption of electrolyte cations (K^+) on the electrode surface from electrolyte. Due to being amphoteric in nature of the iron oxide surface, the electrolyte provides additional charge storage capacity. The capacitive current of iron oxides also originates from the surface reaction as well as the charge compensation accompanied by intercalation of ions to balance the extra charge with the iron oxide layers. On the other hand, low current could be attributed to diffusion limits of electrolyte ions [23, 26]. It was also clear from Fig. 6b that a pair of redox peaks for Fe^{2+}/Fe^{3+} in the range between 0 and 0.85 V were observed as expected. The peak was shifted to higher potential with increase of the scan rates. The gradually increasing peak intensity in cathodic process indicated that the capacities of these electrodes could gradually decrease with increase in scan rate. The presence of the redox peaks

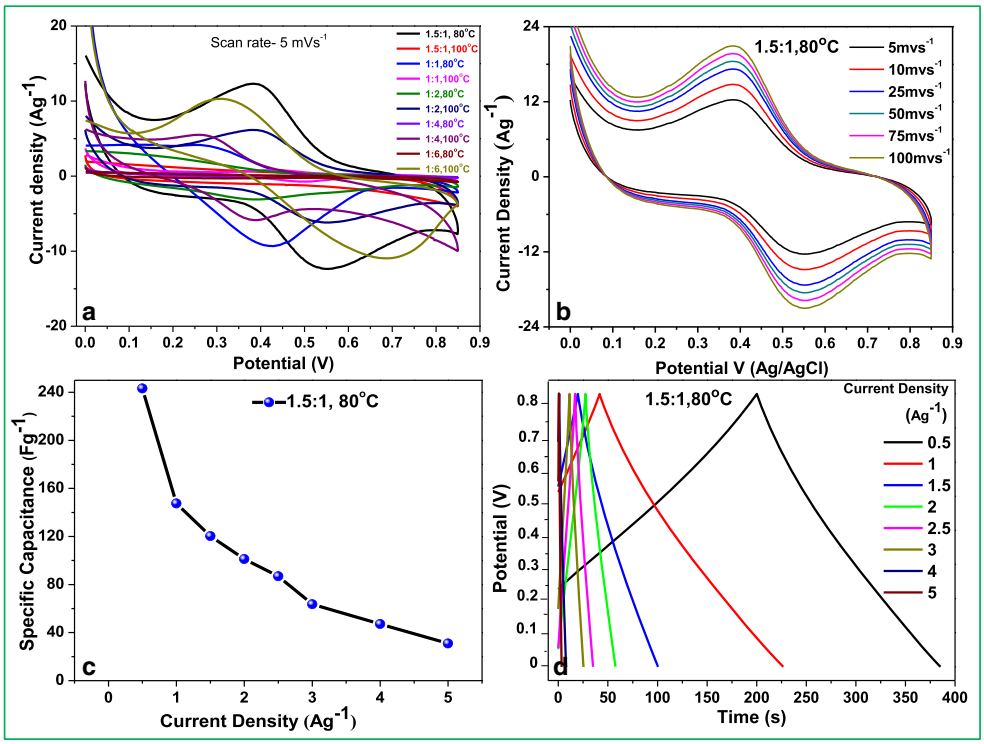

Fig. 6 Electrochemical studies. **a** Cyclic voltammogram of all the materials at a scan rate 5mVs^{-1}. **b** Cyclic voltammogram of 1.5:1, 80 °C, 5 h materials at different scan rate 5 mVs^{-1} to 100 mVs^{-1}. **c** Specific capacitance value of 1.5:1, 80 °C, 5 h material at different current densities. **d** Charge–discharge curves of 1.5:1, 80 °C, 5 h material at different current densities

indicates that the capacitive response comes from the Faradaic redox reactions relating to the Fe–O/Fe–O–OH. The CV nature of the electrode of the sample at 1:1, 1:2, 1:4, and 1:6 at both low and high temperature is of rectangular type and that at higher temperature contain a prominent pair of redox peak as compared to the sample obtained at low temperature [3].

Considering the current density from the Fig. 6a, the sample prepared with 1.5:1 ratio at 80 °C was considered for the further study. The highest SC of 243.2 Fg^{-1} (shown in Fig. 6c) was obtained for the sample prepared with 1.5:1 ratio at 80 °C whereas other samples showed less capacitance by the following Formula 1 [5]. The specific capacitance value was obtained at 0.5 Ag^{-1} current density. Charge–discharge properties of 1.5:1, 80 °C, 5 h material at different current densities was studied and given in Fig. 6d.

$$\text{Specific capacitance Csp } \left(\text{Fg}^{-1}\right) = I\Delta t/m\Delta V \tag{1}$$

where I = supplied current, Δt = discharge time, m = active mass on electrode, and ΔV = operating potential window. Here in this study, the specific capacitance value may depend on the phase formation, morphology, and concentration of salt and solvent. As in the 1.5:1 sample, the concentration of iron was more compared to the solvent. So, the transfer of electrons between Fe^{2+} and Fe^{3+} in the octahedral sites was more which may enhance [13] the specific capacitance at low temperature of 80 °C but at high temperature (100 °C), the rate of electron transfer was less which corresponded to the low specific capacitance value. These were behaving as ideal electrochemical capacitor which do not have current leakage pathway or self-discharge and hence can remain charged indefinitely. Again, porous/net-like structures developed by the fusion/aggregation of spherical particles which have unique architecture resulted in a reduction of the grain boundaries between the particles in comparison to the electrode. Also, it enhances the reduction in internal resistance, which supported the enhanced supercapacitor performance [3, 7, 10, 11, 13, 30, 32, 36].

The cyclic performance of electrodes was also investigated by charge–discharge was given in Fig. 7a. Charge–discharge up to 1000 cycles at current density 3 Ag^{-1} was studied. A retention in specific capacitance of 96.5% after 1000 cycle was obtained. This indicates that the iron oxide showed good cycling stability with almost 100% coulombic efficiency. Thus, it was reasonable to conclude that the capacitance of typical sample mainly comes from the goethite or herein mix phases of iron oxide. Figure 7b (inset) represents the ragone plot for the synthesized material 1.5:1, 80 °C. The material showed 26 Wh Kg^{-1} energy density and power density 32 W Kg^{-1} at 0.5 Ag^{-1} calculated by Formula 2 and 3. The energy density (E) and power density (P) of the asymmetric device was calculated with respect to the specific capacitance value by following formula:

$$\text{Energy density (E)} = I\,dV\,t/m \tag{2}$$

$$\text{Power density (P)} = E/dt \tag{3}$$

Electrochemical impedance spectroscopy (EIS) is another important technique which provides more information

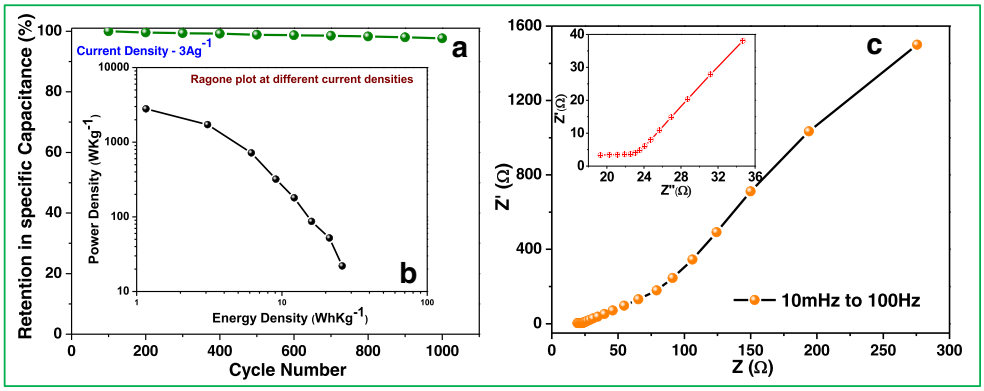

Fig. 7 **a** Cycling stability of iron oxide material (1.5:1, 80 °C) at 3 Ag^{-1} current density up to 1000 cycle. **b** Inset—Ragone plot for iron oxide (1.5:1, 80 °C) at different current densities. **c** EIS curve for iron oxide (1.5:1, 80 °C) sample in the frequency range of 10 mHz to 100 Hz

regarding the electrochemical behavior, property, and nature of the material basing on frequency. The EIS spectra of both the samples were given in Fig. 7c. The Nyquist plots of 1.5:1, 80 °C were obtained from 10 mHz to 100 Hz in a three-electrode cell with Pt as counter and Ag/AgCl as reference electrode. Among them, the FeOOH electrode owns the smallest internal resistance at high frequency region; otherwise, it showed good conductivity. It also showed the faster electron transport in electrode material, which proves FeOOH as the best pseudo-capacitor material.

Conclusions

Herein, the feasibility of fabrication of 3D flowery structured, nearly mono-dispersed iron oxide nanocrystals is discussed via solution process using metalo-organic composite solution. The self-assembling of the goethite nano-flowers was tunable by controlling the composition of the initial reaction mixture of salt and solvent. The formation of flower-like particles went through initial formation of primary nanocrystals, followed by agglomeration of the primary particles to form intermediate nanorods, and finally, the anisotropic growth of the nanorods into flower-like extended structures. This study is quite helpful for developing different phases of flowery-shaped iron oxides along with core–shell flower-like structures by controlling only the solute-to-solvent ratio, which in turn controls both hydrolysis and selective-phase precipitation. The samples were further explored for the electrochemical behavior, which confirms that the iron oxide synthesized under optimum conditions also had a good rate capability. The results demonstrated the excellent reversibility and ideal pseudo-capacitive behavior of the three electrodes. Goethite sample obtained at 1.5:1 at 80 °C showed better specific capacitance value of 243.2 Fg^{-1}. As in this case, the concentration of iron was more as compared to the solvent. So, the transfer of electrons between Fe^{2+} and Fe^{3+} in the octahedral sites was more which may enhance the specific capacitance at low temperature. The iron oxide has 96.5% in retention in specific capacitance up to 1000 cycle with energy density 26 Wh kg^{-1}. The pure iron oxide nanomaterial shows good capacitance along with charge–discharge behavior without further hybridization or the addition of a dopant in nanostructured material. The simple, synthetic, one-step approach to develop the surface and morphology-specific properties of the present materials and the novel fabrication of the electrode offers a promising approach for super capacitors.

Acknowledgements The first author is thankful to the DST Inspire Division (Govt. of India) for their financial support. The Author Mamata Mohapatra is thankful to DST for providing BOYSCAST fellowship. The authors are grateful to Prof. K. Mallick, University of Johannesburg, South Africa, for his kind help to carryout electrochemical and impedance study.

Author contributions The manuscript was written through contributions of all authors. All authors have given approval to the final version of the manuscript.

Funding information This study was funded by the DST Inspire Division (Govt. of India) (first author).

Compliance with ethical standards

Conflict of interest The authors declare that they have no conflict of interest.

References

1. Agarwala S, Lim ZH, Nicholson E, Ho GW (2012) Probing the morphology-device relation of Fe_2O_3 nanostructures towards photovoltaic and sensing applications. Nanoscale 4:194–205. https://doi.org/10.1039/C1NR10856E
2. Baltrusaitis J, Cwiertnya DM, Grassian VH (2007) Adsorption of sulfur dioxide on hematite and goethite particle surfaces. Phys Chem Chem Phys 9:5542–5554. https://doi.org/10.1039/B709167B
3. Barik R, Jena BK, Dash A, Mohapatra M (2014a) In situ synthesis of flowery-shaped α-FeOOH/Fe_2O_3 nanoparticles and their phase dependent supercapacitive behaviour. RSC Adv 4:18827–18834. https://doi.org/10.1039/C4RA01258E
4. Barik R, Pandey B, Anand S, Mohapatra M (2014b) A facile, single-step synthesis of flowery shaped, pure/lithium-doped 3D

iron oxides. J Mater Chem A 2:12380–12389. https://doi.org/10.1039/C4TA00270A
5. Barik R, Jena BK, Mohapatra M (2017) Metal doped mesoporous FeOOH nanorods for high performance supercapacitors. RSC Adv 2017(7):49083–49090. https://doi.org/10.1039/C7RA06731C
6. Beznosov SN, Veluri PS, Pyatibratov MG, Chatterjee A, MacFarlane DR, Fedorov OV, Mitra S (2015) Flagellar filament bio-templated inorganic oxide materials—towards an efficient lithium battery anode. Sci Rep 5:7736–7742. https://doi.org/10.1038/srep07736
7. Binitha G, Soumya MS, Madhavan AA, Praveen P, Balakrishnan A, Subramanian KRV, Reddy MV, Nair VS, Nair AS, Sivakumar N (2013) Engineering of high performance supercapacitor electrode based on Fe-Ni/Fe_2O_3-NiO core/shell hybrid nanostructures. J Mater Chem A 1:11698–11704. https://doi.org/10.1063/1.4913218
8. Cai D, Wang D, Liu B, Wang Y, Liu Y, Wang L, Li H, Huang H, Li Q, Wang T (2013) Comparison of the electrochemical performance of NiMoO4 nanorods and hierarchical nanospheres for supercapacitor applications. ACS Appl Mater Interfaces 5(24):12905–12910. https://doi.org/10.1021/am403444v
9. Cao J, Li G, Wang Y, Sun G, Bala H, Wang X, Zhang Z (2014) Synthesis and characterization of hierarchical porous-FeOOH for the adsorption and photodegradation of rhodamine B. Int J Photoenergy 2014:1–8. https://doi.org/10.1155/2014/468921
10. Cao G, Liu J, Wang Y, Mao L, Fan Z, Shen Z, Zhang H, Wang J (2015) Iron oxide-decorated carbon for supercapacitor anodes with ultrahigh energy density and outstanding cycling stability. ACS Nano 9:5198–5207. https://doi.org/10.1021/acsnano.5b00582
11. Chaudhari S, Bhattacharjya D, Yu JS (2013) 1-Dimensional porous α-Fe_2O_3 nanorods as high-performance electrode material for supercapacitors. RSC Adv 3:25120–25128. https://doi.org/10.1039/C3RA44159H
12. Chen K, Xue D (2013) Room-temperature chemical transformation route to CuO nanowires toward high performance electrode materials. J Phys Chem C 117:22576–22583. https://doi.org/10.1021/jp4081756
13. Chen L-F, Yu Z-Y, Wang J-J, Li Q-X, Tan Z-Q, Zhu Y-W, Yu S-H (2015) Metal-like fluorine-doped β-FeOOH nanorods grown on carbon cloth for scalable high-performance supercapacitors. Nano Energy 11:119–128. https://doi.org/10.1016/j.nanoen.2014.10.005
14. Cornell R M, Giovanoli R (1987) Effect of Manganese on the Transformation of Ferrihydrite into Goethite and Jacobsite in Alkaline Media. Clays and Clay Minerals 35:11–20 https://doi.org/10.1346/CCMN.1987.0350102
15. Hockridge JG, Jones F, Loan M, Richmond WR (2009) An Electron Microscopy Study of the Crystal Growth of Schwertmannite Needles through Oriented Aggregation of Goethite Nanocrystals. J. Cryst. Growth 311:3876-3882. https://doi.org/10.1016/j.jcrysgro.2009.06.023
16. Ito D, Yokoyama S, Zaikova T, Masuko K, Hutchison JE (2014) Synthesis of ligand-stabilized metal oxide nanocrystals and epitaxial core/shell nanocrystals via a lower-temperature esterification process. ACS Nano 8:64–75. https://doi.org/10.1021/nn401888h
17. Jia Y, Yu XY, Luo T, Zhang MY, Liua JH, Huang XJ (2013) Two-step self-assembly of iron oxide into three-dimensional hollow magnetic porous microspheres and their toxic ion adsorption mechanism. Dalton Trans 42:1921–1928. https://doi.org/10.1039/C2DT32522E
18. Jun Y, Yu D, George MC, Braun PV (2010) Holographically defined nanoparticle placement in 3D colloidal crystals. J Am Chem Soc 132:9958–9959. https://doi.org/10.1021/ja1023628
19. Kamat PV, Tvrdy K, Baker DR, Radich JG (2010) Beyond photovoltaics: semiconductor nano architectures for liquid-junction solar cells. Chem Rev 110:6664–6688. https://doi.org/10.1021/cr100243p
20. Kosa SA, Maksod IHAE, Alkhateeb L, Hegazy EZ (2012) Preparation and surface characterization of CuO and Fe_2O_3 catalyst. Appl Surf Sci 258:7617–7624. https://doi.org/10.1016/j.apsusc.2012.04.103
21. Kroes GJ, Gross A, Baerends EJ, Scheffler M, Mc Cormack DA (2002) Quantum theory of dissociative chemisorption on metal surfaces. Acc Chem Res 35:193–200. https://doi.org/10.1021/ar010104u
22. Kumar R, Ozoemena KI (2015) Hierarchical one-dimensional ammonium nickel phosphate microrods for high-performance pseudocapacitors. Sci Rep 5:17629. https://doi.org/10.1038/srep17629
23. Li ZC, Guan MY, Lou ZS, Shang TM (2012) Facile hydrothermal synthesis and electrochemical properties of flowerlike α-FeOOH. Micro Nano Lett 7:33–36. https://doi.org/10.1049/mnl.2011.0511
24. Liao MY, Lai PS, Yu HP, Lin HP, Huang CC (2012) Innovative ligand-assisted synthesis of NIR-activated iron oxide for cancer theranostics. Chem Commun 48:5319–5321. https://doi.org/10.1039/C2CC31448G
25. Ling Y, Wang G, Wheeler DA, Zhang JZ, Li Y (2011) Sn-doped hematite nanostructures for photoelectrochemical water splitting. Nano Lett 11:2119–2125. https://doi.org/10.1021/nl200708y
26. Liu H, Xie J, Wang K (2008) Synthesis and characterization of nano-$LiFePO_4$/carbon composite cathodes from 2-methoxyethanol–water system. J Alloys Compd 459:521–525. https://doi.org/10.1016/j.jallcom.2007.05.031
27. Long C, Jiang L, Wei T, Yan J, Fan Z (2014) High-performance asymmetric supercapacitors with lithium intercalation reaction using metal oxide-based composites as electrode materials. J Mater Chem A 2:16678–16686. https://doi.org/10.1039/C4TA03241A
28. Maiyalagan T, Sundaramurthy J, Kumar PS, Kannan P, Opallo M, Ramakrishna S (2013) Nanostructured α-Fe_2O_3 platform for the electrochemical sensing of folic acid. Analyst 138:1779–1786. https://doi.org/10.1039/C3AN00070B
29. Mao XB, Yang HC, Zhou XM, Wang CX, Wang YS, Yang YL, Wang C, Liu G (2010) Straight and branched goethite topology by oriented attachment at high pH. Cryst Growth Des 10:504–509. https://doi.org/10.1021/cg900392m
30. Mitchell E, Gupta RK, Darkwa KM, Kumar D, Ramasamy K, Gupta BK, Kahol P (2014) Facile synthesis and morphogenesis of superparamagnetic iron oxide nanoparticles for high-performance supercapacitor applications. New J Chem 38:4344–4350. https://doi.org/10.1039/C4NJ00741G
31. Pierre AC (1998) Introduction to sol-gel processing, Kluwer Acad. Pub.mNew York, USA
32. Reddy MV, Jose R, Teng TH, Chowdari BVR, Ramakrishna S (2010) Preparation and electrochemical studies of electrospun TiO_2 nanofibers and molten salt method nanoparticles. Electrochim Acta 55:3109–3117. https://doi.org/10.1016/j.electacta.2009.12.095
33. Rieke P C, Marsh B D, Wood L L, Tarasevich B J, Liu J, Song L, Fryxell G E(1995) Aqueous Solution Deposition Kinetics of Iron Oxyhydroxide on Sulfonic Acid Terminated Self-Assembled Monolayer. Langmuir 11:318-326. https://doi.org/10.1021/la00001a054
34. Rout K, Mohapatra M, Layek S, Dash A, Verma HC, Anand S (2016) The influence of precursors on phase evolution of nano iron oxides/oxyhydroxides: optical and magnetic properties. New J Chem 38:3492–3506. https://doi.org/10.1039/C4NJ00526K.
35. See TP, Pandikumar A, Ming HN, Ngee LH, Sulaiman Y (2014) Simultaneous electrochemical detection of dopamine and ascorbic acid using an iron oxide/reduced graphene oxide modified glassy carbon electrode. Sensors 14:15227–15243. https://doi.org/10.3390/s140815227

36. Shivakumara S, Penki TR, Munichandraiah N (2014) High specific surface area α-Fe_2O_3 nanostructures as high-performance electrode material for supercapacitors. Mater Lett 131:100–103. https://doi.org/10.1016/j.matlet.2014.05.160
37. Suresh R, Giribabu K, Manigandan R, Vijayaraj A, Prabu R, Stephen A, Narayanan V (2014) α-Fe_2O_3 nanoflowers: synthesis, characterization, electrochemical sensing and photocatalytic property. J Iran Chem Soc 11:645–652. https://doi.org/10.1007/s13738-013-0335-0
38. Tanggarnjanavalukul C, Phattharasupakun N, Kongpatpanich K, Sawangphruk M (2017) Charge storage performances and mechanisms of MnO_2 nanospheres, nanorods, nanotubes and nanosheets. Nanoscale 9:13630–13639. https://doi.org/10.1039/c7nr02554h.
39. Wang Y, Ma J, Chen K (2013) Adsorptive removal of Cr(VI) from wastewater by α-FeOOH hierarchical structure: kinetics, equilibrium and thermodynamics. Phys Chem Chem Phys 15:19415–19421. https://doi.org/10.1039/c3cp52867g
40. Xia Q, Xu M, Xia H, Xie J (2016) Nanostructured iron oxide/hydroxide-based electrode materials for supercapacitors. ChemNanoMat 2:588–600. https://doi.org/10.1002/cnma.201600110
41. Zeng HC (2007) Oriented attachment: a versatile approach for construction of nanomaterials. Int J Nanotechnol 4:329–346. https://doi.org/10.1504/IJNT.2007.013970
42. Zhang L, Wu HB, Lou XW (2014) Iron-oxide-based advanced anode materials for lithium-ion batteries. Adv Energy Mater 4:1300958–1300967. https://doi.org/10.1002/aenm.201300958
43. Zhang M, Chen K, Chen X, Peng X, Sun X, Xue D (2015) Crystallization of FeOOH via iron salts: an anion-chemo affinity controlled hydrolysis toward high performance inorganic pseudo capacitor materials. Cryst Eng Comm 17:1917–1922. https://doi.org/10.1039/C4CE02543A
44. Zhang S, Li C, Xiao H, Wei G, Zhou Y, Wang Z, Zhang J, An C (2017) Synthesis of 3D flower-like cobalt sulfide hierachitecture for high-performance electrochemical energy storage. J Nanopart Res 19:202. https://doi.org/10.1007/s11051-017-3905-8
45. Zhao Y, Chen S, Sun B, Su D, Huang X, Liu H, Yan Y, Sun K, Wang G (2015) Graphene-Co3O4 nanocomposite as electro catalyst with high performance for oxygen evolution reaction. Sci Rep 5:7629–7635. https://doi.org/10.1038/srep07629
46. Zhong LS, Hu JS, Liang HP, Cao AM, Song WG, Wan LJ (2006) Self-assembled 3D flowerlike iron oxide nanostructures and their application in water treatment. Adv Mater 18:2426–2431. https://doi.org/10.1002/adma.200600504
47. Zhu LP, Xiao HM, Liu XM, Fu SY (2006) Template-free synthesis and characterization of novel 3D urchin-like α-Fe_2O_3 superstructures. J Mater Chem 16:1794–1797. https://doi.org/10.1039/B604378J